A High Resolution Scanning Pencil-Beam Scatterometer: System Design Challenges

Prantik Chakraborty, Priyanka Gupta, Tapan Misra
Space Applications Centre, ISRO, Satellite Road, Ahmedabad – 380058, India

ABSTRACT

The scanning pencil-beam Scatterometer configuration is pretty effective in covering a large ground-swath by rotating a moderately sized paraboloid dish at a moderate speed. For example, Oscat (Oceansat-II Scatterometer) did cover a ground-swath of 1550km using a 1m diameter reflector that was rotated at 20.5 rpm [1]. The decade-long service (1999—2009) provided by the Seawinds instrument onboard the Quikscat mission followed by an almost half-a-decade (2009—2014) service of Oscat has made this configuration tremendously popular with the global user community. A major drawback of conventional pencil-beam systems like Seawinds and Oscat is the relatively poor spatial resolution. The ground-resolution is beamwidth-limited azimuthally while, in elevation, the resolution is improved by engaging pulse-compression and range-binning. Oscat's Instantaneous Field of View (IFOV) was 25km wide in azimuth (az) and 50km in elevation (el) at 49^0 incidence angle. The range-compressed resolution bins had dimensions of 6km (el) x 25km (az). Therefore, qualified wind products could be generated upon square grids no finer than 25km x 25km resolution. According to recommendations of International Ocean Vector Wind Science Team (IOVWST) and Oscat user community, high-resolution scatterometry is the requirement of the day with wind-vector cell-size dimension of 5km or better. One way to improve the resolution is to adopt the SAR principle of Range-Doppler discrimination in the scanning pencil-beam configuration. The footprint can be resolved simultaneously in range as well as in azimuth, thus significantly improving the size of the combined Range-Doppler resolution bin (~ 1km). However, the addition of Doppler filtering to conically scanning radar brings with it its own disadvantages e.g. the limitations of dwell time and the constant change in orientation of isodop lines. This paper presents the constraints in system design of high-resolution scanning systems, the design trade-offs, the methods of handling high PRF, the radar pulsing scheme and the achievable resolution.

Keywords: Range-Doppler discrimination, Ambiguity, Along-Track Continuity, Scanning Loss, Beamwidth, Pulse-Burst Technique, Spatial Resolution

1. INTRODUCTION

Pencil-beam Scatterometers have some definite advantages over their fan-beam counterparts. It is relatively easy to accommodate on a spacecraft a single rotating paraboloid dish than multiple large fan-beam antennas. This apart, from the perspective of science and applications, the large contiguous swath at constant incidence angle of the conically scanning pencil-beam geometry is more desirable than limited-swath with varying incidence angle of the fan-beam systems. On the other hand, the fan-beam geometry can afford finer spatial resolution via virtue of Range-Doppler filtering [3]. The European Space Agency (ESA) maintains its pre-occupation with C-band scatterometry and its legacy of fan-beam systems beginning with the ERS Scatterometers and now continuing with the Advanced Scatterometer (AScat) series. NASA started off with fan-beam Scatterometers at Ku-band in Seasat and NScat, but switched over to pencil-beam scanning system with the Seawinds instrument onboard the ADEOS-II and Quikscat missions. Recently Rapidscat, a Quikscat-like Scatterometer, has been put up on the ISS platform. Oscat was ISRO's first pencil-beam scanning Scatterometer in space [1]. Scatsat-1, a quick replacement of Oscat, will be launched in 2016. A high-resolution scanning Scatterometer is being envisaged for ISRO's next generation ocean observation satellite series.

Conventional pencil-beam Scatterometers are real-aperture radars which, in spite of employing pulse-compression for range resolution enhancement, ultimately depend upon the antenna beamwidth for the azimuthal resolution and hence,

Remote Sensing of the Oceans and Inland Waters: Techniques, Applications, and Challenges,
edited by Robert J. Frouin, Satheesh C. Shenoi, K. H. Rao, Proc. of SPIE Vol. 9878, 98780R
© 2016 SPIE · CCC code: 0277-786X/16/$18 · doi: 10.1117/12.2228162

are generally low-resolution systems. Quikscat delivered wind-vector products over 25km square grids. Oscat promised 50km gridded winds but, finally achieved 25km. The committed wind–grid resolution for Oscat's successor Scatsat-1 is 25km. This is too coarse a resolution for observing the shape and extent of a cyclone's eye and also for going near the coast and predicting a cyclone's landfall. Improvement by a factor of 2 (~ 10km) is essential and a factor of 5 (~ 5km) is desirable for observing highly dynamic structures such as tropical cyclones, identifying their genesis and predicting their track and landfall. Oscat could deliver uncontaminated wind products 50km away from coast with an uncertainty of ±25km. It is essential to observe within 10km off a sea-coast for issuing early warning for commercial fisheries and maritime navigation.

Post-processing techniques such as the Scatterometer Image Reconstruction (SIR) [2] algorithm have been attempted to improve upon the beam-width limited resolution of pencil-beam Scatterometers. Such techniques exploit the redundancy of information in multiple overlapping measurements in order to resolve the original high-resolution backscatter coefficient of the background scene. These are "multi-pass" techniques and the observations involved are temporally apart and azimuthally diverse. Therefore, such techniques are not viable in the operational sense over ocean surface which is naturally highly dynamic (Oscat data has a turnaround time of 3 hours from data acquisition to dissemination beyond which the data were considered unsuitable for assimilation in the NWP models) and also limits application over land surface because of the presumption that the scene is azimuthally isotropic. Such techniques are maximally successful in the polar regions which are temporally quite stable, topographically homogeneous and have the privilege of a large number of overpasses each day. However, Scatterometers are primarily ocean-observing and wind sensing instruments in near real time and hence, should be equipped with inherent real-time high resolution observation capability. In other words, the problem should be targeted from the instrument perspective. An obvious approach is to adopt the principle of its cousin, the Synthetic Aperture Radar (SAR), in its conically scanning geometry.

The concept of adopting SAR observation and processing principle in the conically scanning Scatterometer configuration is illustrated in Section 2. The design challenges and the trade-offs in system parameters of a high resolution Scatterometer are discussed at length in Section 3. The radar pulsing scheme required to implement Range-Doppler discrimination is addressed in Section 4. The finer resolution that can be achieved by this technique is shown in Section 5.

2. CONCEPT OF RANGE-DOPPLER DISCRIMINATION IN SCANNING SYSTEMS

Unlike conventional SAR systems, the exposure (or dwell) time of a given scene in case of a scanning system is constrained by the scanning rate and the width of the IFOV. The maximum Doppler bandwidth that can be resolved at an arbitrary azimuth is limited to that of the instantaneous footprint. This also puts a limit on the finest achievable spatial resolution. An interesting way of visualizing the Range-Doppler discrimination in case of scanning geometry is to superimpose the IFOVs along a scan at diverse scan (or azimuth) angles upon the iso-range and iso-Doppler contours across the measurement swath (refer Figure 1). The iso-range and isodop lines are generated based upon the Oscat (as well as Scatsat-1) orbit nominal altitude (720 km) and look angle (42.62^0).

It can be seen that the iso-range and isodop contours intersect perpendicularly when the antenna beam is side-looking i.e. 90^0 or 270^0 cross-track. As the antenna is rotated towards the direction of spacecraft motion (forward-looking i.e. 0^0 azimuth when the beam is aligned with the positive velocity vector, and aft-looking when it is pointing 180^0 opposite), the Doppler contours tend to become parallel with the range contours. An IFOV can be resolved at any azimuth position into resolution-bins which are delimited by intersection of the range and Doppler contours (see Figure 1). Such bins are rectangular at the swath edge (side-looking case) and get distorted into parallelograms as the iso-range and isodop contours intersect at acute angles (between 90^0 and 0^0) from the swath-edge to the swath-centre (fore- or aft-looking case). Therefore, the best possible resolution can be achieved at the swath-edge. The elongation of resolution bins from neat rectangles to stretched parallelograms results in degradation of resolution across the swath. The resolution degradation is further worsened by the fact that the isodop hyperbolas curve away from one another with increasing distance from the nadir thus, further stretching the parallelograms. In the vicinity of the sub-satellite trace i.e. fore-/aft-looking cases, the Range-Doppler discrimination is no longer possible and the resolution once again becomes beamwidth-limited.

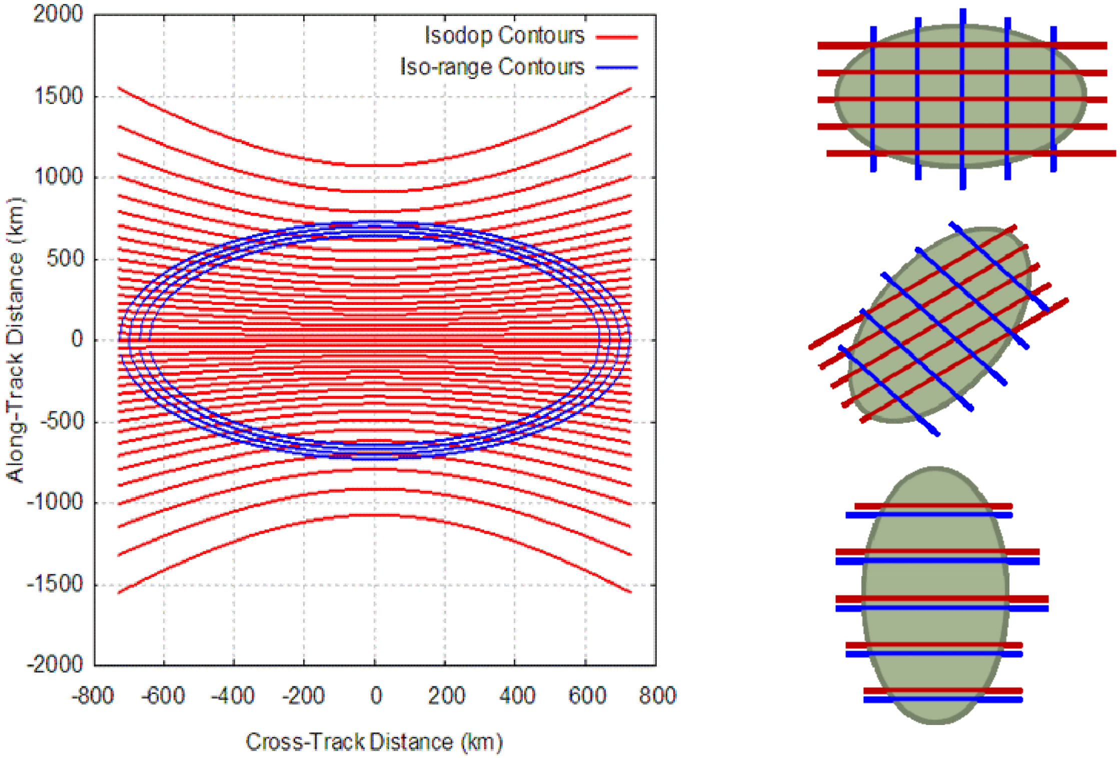

Figure 1. Left: Iso-range and isodop curves across the swath; Right: Intersection of iso-range and isodop curves within a footprint at swath-edge, middle of the swath and at near the sub-satellite track.

In spite of all these limitations, the resolution enhancement that can be attained by Range-Doppler discrimination is an order of magnitude better than that achieved with conventional scanning Scatterometers for a major portion of the swath. This is illustrated in Section 5. The variation of spatial resolution across the swath can be modeled by formulating the spatial gradient of the isodop contours in elevation and azimuth directions. Since the iso-range lines are locally parallel to the footprint azimuth axis, the angle between the elevation and azimuth gradients of the isodop contours is a measure of the angle between the isodop and iso-range lines at any azimuth position. The elevation component of the first derivative of Doppler frequency is formulated in Equations 1—3.

$$f_{DC} + \Delta f_D\big|_{el} = \frac{2v_{sc}}{\lambda}\sin\left(\theta_{look} + \Delta\theta_{el}\right)\cos\theta_{az} \tag{1}$$

$$\left(f_{DC} + \Delta f_D\big|_{el}\right) - f_{DC} \cong \frac{2v_{sc}\Delta x_{el}}{\lambda R}\cos\theta_{inc}\cos\theta_{look}\cos\theta_{az} \tag{2}$$

$$\frac{\Delta f_D}{\Delta x_{el}} \cong \frac{2v_{sc}}{\lambda R}\cos\theta_{inc}\cos\theta_{look}\cos\theta_{az} \tag{3}$$

Here, f_{DC} is the Doppler-centroid frequency at an azimuth angle θ_{az} (with respect to the sub-satellite trace) and for antenna pointing angle θ_{look} (with respect to the spacecraft yaw axis). The spacecraft velocity is v_{sc}, the radar range to the target is R, the operating wavelength at Ku-band is λ and the local incidence angle is θ_{inc}. $\Delta f_D\big|_{el}$ is the incremental Doppler shift due to an infinitesimal change in elevation angle $\Delta\theta_{el}$ and the corresponding spatial shift Δx_{el} in the local elevation direction. In a similar fashion, the incremental Doppler shift in azimuth is formulated in Equations 4—6.

$$f_{DC} + \Delta f_D\big|_{az} = \frac{2v_{sc}}{\lambda}\sin\theta_{look}\left[\cos(\theta_{az} + \Delta\theta_{az})\right] \tag{4}$$

$$\begin{aligned}\left(f_{DC} + \Delta f_D\big|_{az}\right) - f_{DC} &\cong -\frac{2v_{sc}}{\lambda}\sin\theta_{look}\Delta\theta_{az}\sin\theta_{az} \\ &= -\frac{2v_{sc}}{\lambda}\sin\theta_{look}\left(\frac{R_g}{R}\Delta\beta_{az}\right)\sin\theta_{az} \\ &= -\frac{2v_{sc}}{\lambda R}\Delta x_{az}\sin\theta_{az}\end{aligned} \tag{5}$$

$$\frac{\Delta f_D}{\Delta x_{az}} \cong -\frac{2v_{sc}}{\lambda R}\sin\theta_{az} \tag{6}$$

Here, $\Delta\beta_{az}$ is the incremental change in the rotation angle of the antenna corresponding to $\Delta\theta_{az}$ shift in the azimuth on surface and these two are related by the factor (R_g / R) where R_g is the distance along surface from the sub-satellite point to the target. The angle χ between the elevation and azimuth components of the spatial gradient is derived in Equation 7. The elongation of the rectangular resolution bin into a parallelogram can be quantified by the cosine of χ (Equation 8).

$$\chi = \tan^{-1}\left({\partial f_D / \partial x_{el}} \Big/ {\partial f_D / \partial x_{az}} \right) \tag{7}$$

$$f_{ang}(\theta_{az}) = 1 \big/ \cos\chi \tag{8}$$

The magnitude of the spatial gradient of isodop contour is formulated in Equation 9. The elongation of this gradient as function of the azimuth angle with respect to the broadside (90^0 cross-track) is represented in Equation 10.

$$f_{grad}(\theta_{az}) = \left[\left(\partial f_D / \partial x_{el}\right)^2 + \left(\partial f_D / \partial x_{az}\right)^2\right]^{1/2} \tag{9}$$

$$f_{isodop\_spacing}(\theta_{az}) = \frac{f_{grad}(\theta_{az})}{f_{grad}(\theta_{az} = 90^0)} \tag{10}$$

The elongations due to angular re-orientation of Doppler contours, $f_{ang}(\theta_{az})$ and that due to increased spacing between isodop curves, $f_{isodop\_spacing}(\theta_{az})$ and the combined effect of both $f_{ang}(\theta_{az})\ f_{isodop\_spacing}(\theta_{az})$ are illustrated in Figure 2. The curves represent the resolution elongation across the swath with respect to the cross-track case. The resolution degrades by factor of 2 at mid swath (350 km cross-track), by factor 4 at quarter swath (175 km cross-track) and becomes asymptotic near the sub-satellite track where it is limited by the beamwidth.

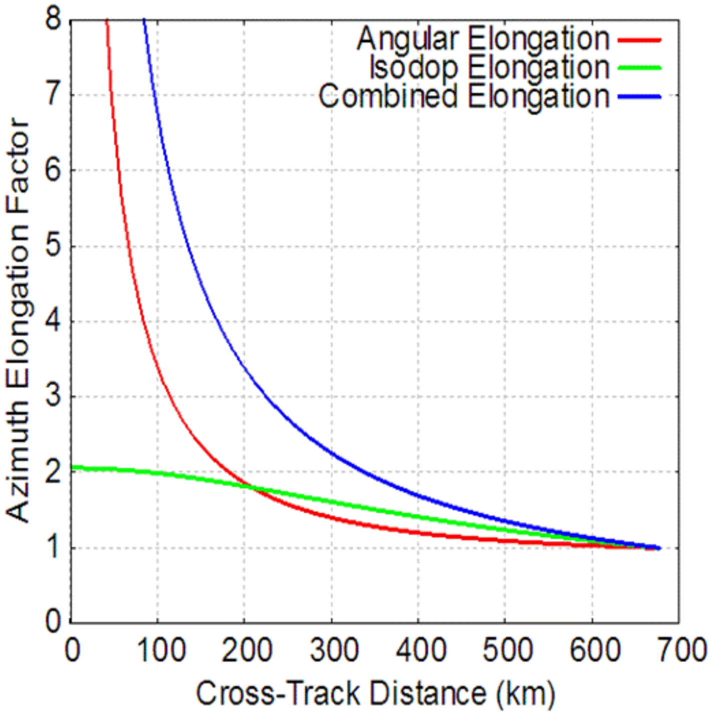

Figure 2. Elongation of azimuth resolution across of the swath on account of azimuth angle, isodop spacing and the combination of both.

3. CONSTRAINTS OF HIGH RESOLUTION SCANNING SYSTEM AND DESIGN TRADE-OFFS

A fundamental design challenge of conically scanning real-aperture Scatterometers is to strike a balance between along-track continuity and the scanning loss in determining the scanning rate. These two factors are related to the beamwidth through the scanning rate. The challenge is aggravated when the beamwidth is further constrained by the requirements of ambiguity suppression once we resort to Range-Doppler discrimination and its corollary, the higher Pulse Repetition Frequencies (PRFs). These factors are mathematically derived and the design trade-offs are addressed in this section.

3.1 Along-Track Continuity

An essential requirement of scanning systems is to ensure gapless coverage of the entire swath during transitions between two consecutive rotations of the antenna. Geometrically it means that the displacement of the sub-satellite point in the duration of a scan should not exceed the elevation width of the IFOV. The along-track continuity constraint may be represented as a factor of overlap η_{el} of footprints in two consecutive scans along the sub-satellite track. This is illustrated in Equation 11.

$$\begin{aligned}\eta_{el} &= \frac{v_g T_{scan}}{x_{el}} \\ &= \frac{v_g T_{scan} \cos\theta_{inc}}{R\beta_{el}}\end{aligned} \tag{11}$$

Here v_g is the spacecraft ground trace velocity, T_{scan} the scan period, β_{el} the elevation beamwidth and x_{el} the elevation width of the footprint. This equation establishes an inverse relation between T_{scan} and β_{el} or, in other words, puts a higher limit on the elevation beamwidth of the antenna for feasible scan rates in order to maintain along-track continuity. We have reached the maximum elevation beamwidth or, equivalently the minimum antenna dimension criterion.

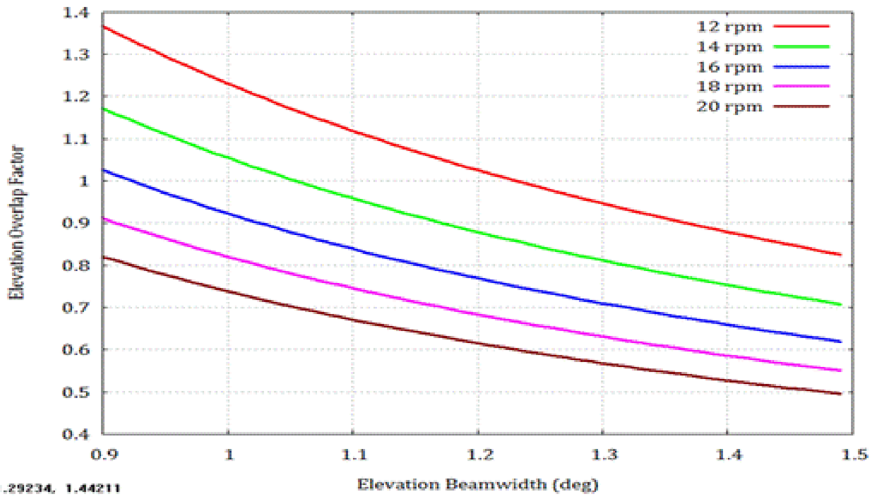

Figure 3. Elevation beamwidth versus elevation overlap factor for a range of scan-rates at intervals of 2 rpm

The elevation overlap factors have been plotted as function of elevation beamwidth for a range of scan-rates at regular intervals in Figure 3. It can be seen that along-track continuity is maintained $(\eta_{el} < 1)$ for scan-rate 16 rpm or higher if the elevation beamwidth is as low as 1^0 (roughly corresponding to 1.5 m diameter dish; Oscat had a 1m dish).

3.2 Scanning Loss

This element is a major factor in determining the spin-rate of scanning radar systems. The antenna gain pattern during radar transmit and receive events are mutually offset by the angle which the scanner describes in the duration of round-trip transit of the radar pulse. Scanning loss is the decrease in transmit-receive gain product on account of this angular offset and is expressed as the ratio of integrated transmit-receive gain product in presence and absence of such offset. This is illustrated in Equation 12.

$$L_{scan} = \frac{\iint\limits_{\beta_{el},\beta_{az}} G(\phi_{el},\phi_{az}) G\left(\phi_{el},\phi_{az} + \frac{2R}{c}\omega_{scan}\sin\theta_{look}\right) d\phi_{el} d\phi_{az}}{\iint\limits_{\beta_{el},\beta_{az}} G^2(\phi_{el},\phi_{az}) d\phi_{el} d\phi_{az}} \qquad (12)$$

Here $G(\phi_{el},\phi_{az})$ is the antenna gain at an elevation angle ϕ_{el} and azimuth angle ϕ_{az} and the angular movement of the scanner during the roundtrip transit time $\frac{2R}{c}$ is $\frac{2R}{c}\omega_{scan}\sin\theta_{look}$. The scanning loss is plotted as function of azimuth beamwidth in Figure 4 for the same set of scan-rates as shown in Figure 3. It can be seen that for smaller azimuth beamwidths (e.g. 1^0) and/or higher spin rates (20rpm, the Oscat example), the scanning loss can be significantly high and erode the system SNR. Therefore, for a given spin-rate, scanning loss determines the minimum azimuth beamwidth or, equivalently, the maximum azimuth antenna dimension. Here, we introduce an azimuth overlap factor η_{az} (in the lines of the elevation overlap factor in Equation 11) which relates the spin-rate to azimuth beamwidth. Understandably, the spin-rate is the representative of an acceptable scanning loss for a given azimuth beamwidth in Equation 13.

$$\eta_{az} = \frac{\frac{2R}{c}\omega_{scan}R_g}{x_{az}} = \frac{2\omega_{scan}R_g}{c\beta_{az}} = \frac{4\pi R_g}{c\beta_{az}T_{scan}} \tag{13}$$

$$\beta_{az}\beta_{el} = \frac{4\pi v_g R_g \cos\theta_{inc}}{cR\eta_{az}\eta_{el}} \tag{14}$$

Combining equations 11 and 13, we can arrive at an antenna area constraint (elevation-azimuth beamwidth product) as shown in Equation 14. The elements in the right hand side of Equation 14 are all constants except η_{az} and η_{el}. If we freeze η_{az} to limit scanning loss and η_{el} to ensure along-track continuity, we can deduce design curves of β_{az} versus β_{el} as shown in Figure 5. This curves are extremely significant in determining the operating point over a range of elevation and azimuth beamwidth combinations. We will see in Sections 3.3 and 3.4 how we can arrive at a similar set of curves from the Range-Doppler ambiguity constraints.

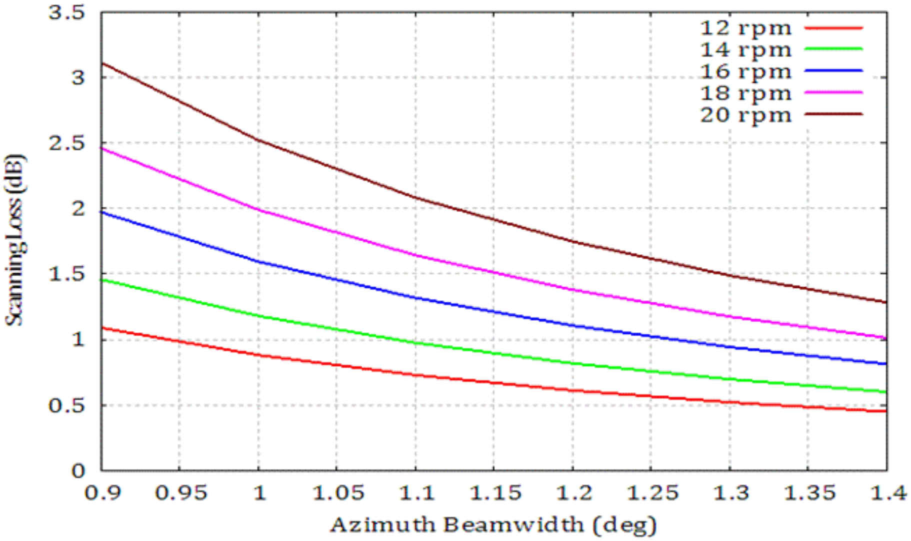

Figure 4. Azimuth beamwidth versus scanning loss for a range of scan-rates at intervals of 2 rpm

3.3 Range Ambiguity

Conventional scanning pencil beam Scatterometers operate at such PRFs in which range ambiguities are never a major concern. For high resolution Scatterometers operating at high PRFs, there will be several preceding and succeeding pulses in flight before the echo of a given transmission is received. Therefore, returns from different pulses and viewing different scenes may arrive simultaneously resulting in ambiguities. The range ambiguity is modelled as the ratio of the echo power levels arriving from different radar ranges (corresponding to multiples of PRIs) and correspondingly weighed by the antenna gain pattern (see Equation 15).

$$Amb_{Ra} = \frac{G^2(\phi_{el} \pm \Delta\phi_{el}(nPRI))}{G^2(\phi_{el})} \times \frac{R^2(\phi_{el})}{R^2(\phi_{el} \pm \Delta\phi_{el}(nPRI))} \times \frac{\cos\theta_{inc}(R \pm \Delta R)}{\cos\theta_{inc}(R)} \tag{15}$$

The radar PRI should oversample the beam-filling time by a factor κ_{el} which controls the ambiguities arising from preceding and succeeding echoes. This is illustrated in Equation 16.

$$PRI = \left\lceil \frac{2\kappa_{el}\Delta R}{c} \right\rceil = \left\lceil \frac{2\kappa_{el}\Delta x_{el}\sin\theta_{inc}}{c} \right\rceil \tag{16}$$

3.4 Doppler Ambiguity

An essential criterion of Doppler discrimination is that the Doppler bandwidth be sampled at Nyquist rate in order to minimize the Doppler ambiguities. The maximum Doppler bandwidth of a pencil beam Scatterometer at 90^0 cross-track is derived in Equations 17—19. It is apparent that the Doppler bandwidth is a linear function of the azimuth beamwidth.

$$\Delta f_{dop}\,|_{\theta_{az}=90^0} = \frac{2v_{sc}}{\lambda}\sin\theta_{look}\left[\cos(\theta_{az} + \Delta\theta_{az}/2) - \cos(\theta_{az} - \Delta\theta_{az}/2)\right] \tag{17}$$

$$= \frac{2v_{sc}}{\lambda}\sin\theta_{look}\Delta\theta_{az} \tag{18}$$

$$= \frac{2v_{sc}}{\lambda}\beta_{az} \tag{19}$$

The radar PRF should oversample the Doppler bandwidth by a factor which controls the azimuth ambiguity. This is represented in Equation 20.

$$PRF = \kappa_{az}\Delta f_{dop} \tag{20}$$

Combining Equations 16 and 20 and realizing that $PRF \times PRI = 1$, we arrive at Equation 21 in which a second condition on the antenna area is delimited.

$$\begin{aligned} PRI \times PRF &= \frac{2\kappa_{el}\Delta x_{el}\sin\theta_{inc}}{c}\frac{2\kappa_{az}v_{sc}}{\lambda}\beta_{az} \\ \Rightarrow \beta_{el}\beta_{az} &= \frac{c\lambda\cot\theta_{inc}}{4v_{sc}R\kappa_{el}\kappa_{az}} \end{aligned} \tag{21}$$

As in Equation 14, the elements on the right hand side of the above equation are all constants except κ_{el} and κ_{az} which are regulators of range and azimuth ambiguity levels respectively. So, one can deduce design curves of β_{az} versus β_{el} by incorporating the necessary ambiguity suppression factors in the forms of κ_{el} and κ_{az}. The antenna beamwidth design curves derived from two separate sets of constraints in Equations 14 and 21 respectively are plotted together in Figure 5. It can be seen that for a single elevation beam, the curves are apart and do not give us a common solution. The curves almost follow each other when a combination of two closely spaced beams in elevation are used to maintain along-track continuity. However, this scheme puts in jeopardy the basic conical Scatterometer principle of having two beams at different incidence angles in order to achieve the azimuthal diversity. On the other hand, the azimuth-elevation ambiguity constraint may be addressed by using certain types of signals in successive pulses which will be mutually uncorrelated upon compression (e.g. reversed chirp slopes) and provide ambiguity suppression and hence, the dependence upon antenna pattern will diminish. These are some of the design trade-offs that are to be taken up additionally in order to achieve requisite system performance.

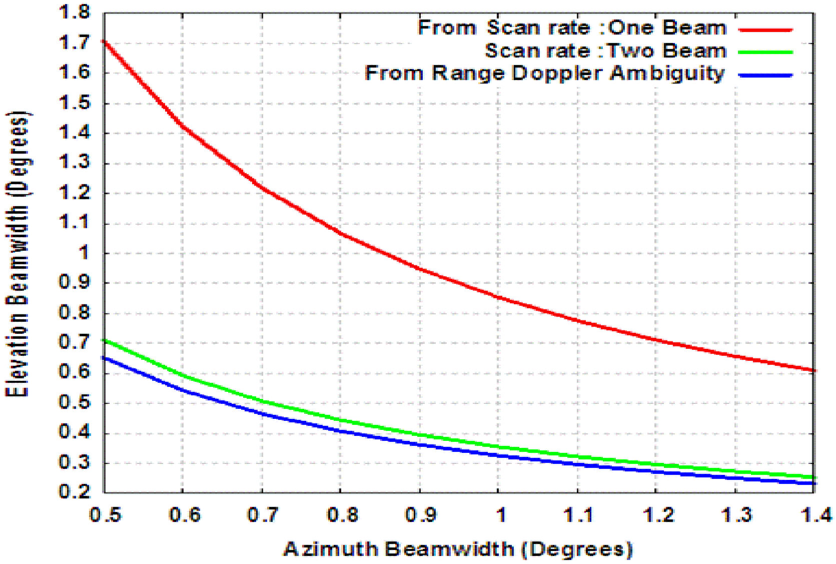

Figure 5. Design curves of azimuth versus elevation beamwidth derived from Range-Doppler ambiguity constraints as well as along-track continuity and scanning loss constraints

4. PULSE-BURST TIMING SCHEME

The pulsing scheme of conically scanning real aperture radar like Oscat is tuned to accommodate the roundtrip transit times of the radar pulses, the echo-width and the dwell time of the scanner per footprint. Oscat had a simple pulse-timing arrangement in which transmit and receive events were interleaved and there were no pulses in flight till the echo from previous transmission is received. However, in order to negotiate the radar pulse transit time with the rotation rate, transmission and reception of the two polarizations were alternated. The Oscat-like pulse timing can be slightly tweaked to make room for the higher PRF necessitated by our high resolution system. Here, we introduce the pulse-burst timing scheme. A number of short pulses may be transmitted within the duration of what happens to be a single pulse in the real aperture case. The erstwhile pulse becomes a burst, the erstwhile PRI become Burst Repetition Interval (BRI) and the new PRI corresponds to the short pulse within the burst. Transmit and receive bursts can then be interleaved with alternating polarizations. This concept is schematically represented in Figure 6.

The fundamental constraint of interleaving the transmit and receive events applies to the entire burst here instead of a single pulse as with conventional pencil-beam scanning Scatterometers. This condition is summarized in Equation 22. It states that two consecutive transmit events should be sufficiently apart in time (the BRI) in order to accommodate the transmit and echo burst lengths.

$$\begin{aligned} BRI &\geq \left(\tau_{burst} + n\left(\tau_{pulse} + \frac{2\Delta R}{c}\right)\right) \\ &\geq \left((n-1+\mu)PRI + n\left(\mu PRI + \frac{2\Delta R}{c}\right)\right) \end{aligned} \tag{22}$$

Here τ_{burst} is the transmit burst duration which comprises of n pulses. Each transmit pulse-width is τ_{pulse} which is related to the PRI through the duty-cycle parameter μ. The echo of each individual pulse has a duration of $\left(\tau_{pulse} + \frac{2\Delta R}{c}\right)$ where ΔR is the difference in radar range to the nearest and farthest points of the one-way 3-dB footprint and $\frac{2\Delta R}{c}$ is the beam-filling time.

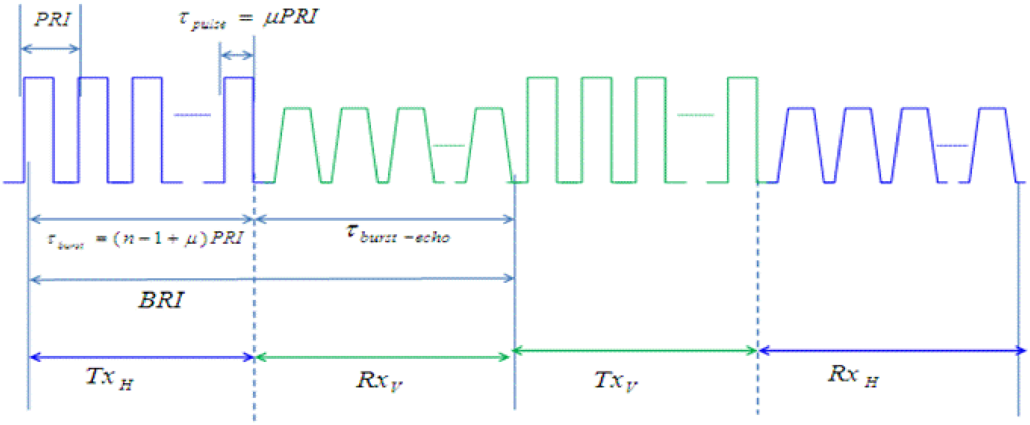

Figure 6. Schematic representation of pulse-burst timing scheme.

The first constraint warrants that the transmission of a pulse-burst does not conflict with the reception of an echo burst. However, it is not only the echo-width that matters; its time of arrival has to be fit in the timing scheme. Therefore, the computation of BRI must take into radar round-trip times from near and far fringes of the footprint. Also, as evident in Figure 6, the two beams at two distinct polarizations are alternated at consecutive BRIs. This means that the burst repetition period for each individual beam (which in essence is twice the system BRI) should satisfy its corresponding round-trip times. Equation 23 states that the transmission of pulse-burst of an individual beam should be repeated only after the entire echo-burst from its previous transmission is received. This constraint puts the farthest limit on the BRI. The nearest limit is set by Equation 24 which states the transmission of a pulse-burst should be over before the echoes from its immediate predecessor start arriving (refer Figure 6). Of course, the first echo corresponds to the near-range roundtrip time which is denoted as $T_{near-range,roundtrip}$.

$$\begin{aligned} 2BRI &\geq \left(T_{near-range,roundtrip} + n\left(\tau_{pulse} + \frac{2\Delta R_{far-beam}}{c}\right)\right) \\ \Rightarrow BRI &\geq \frac{1}{2}\left[T_{near-range,roundtrip} + n\left(\mu PRI + \frac{2\Delta R_{far-beam}}{c}\right)\right] \end{aligned} \tag{23}$$

$$BRI \leq \left(T_{near-range,roundtrip} - \tau_{burst}\right) \tag{24}$$

Equations 23 and 24 respectively define the second and third pulse-burst timing constraints. The fourth and final constraint is specifically introduced to emulate SAR-processing in scanning pencil-beam geometry. The area which is swept by all pulses in a burst can only be resolved in Doppler space and one needs to maintain along-scan continuity of such Doppler-resolved areas. This severely limits the dwell-time per footprint and consequently the azimuth resolution and also shrinks the BRI beyond the limits set by Equation 24. The along-scan continuity constraint is summarized in Equations 25 and 26.

$$2BRI \le \left(\frac{x_{az} - \omega_{scan} R_G \tau_{burst}}{\omega_{scan} R_G}\right) \tag{25}$$

$$\Rightarrow BRI \le \frac{1}{2}\left(\frac{R\beta_{az}}{\omega_{scan} R_G} - (n - 1 + \mu)PRI\right) \tag{26}$$

Here, x_{az} is the azimuth footprint width, $x_{az} - \omega_{scan} R_G \tau_{burst}$ is the area of interest which is viewed by the entire pulse-burst and $\left(\frac{x_{az} - \omega_{scan} R_G \tau_{burst}}{\omega_{scan} R_G}\right)$ is the ground sweep time of the Doppler-space.

An appreciation of how all these constraints limit our choice of the BRI can be derived from Figure 7. BRI curves generating from each one of these constraints have been plotted versus the number of pulses in the burst. It is simple to derive the operating BRI with maximized number of pulses from these curves before the stay-below and stay-above constraints violate each other.

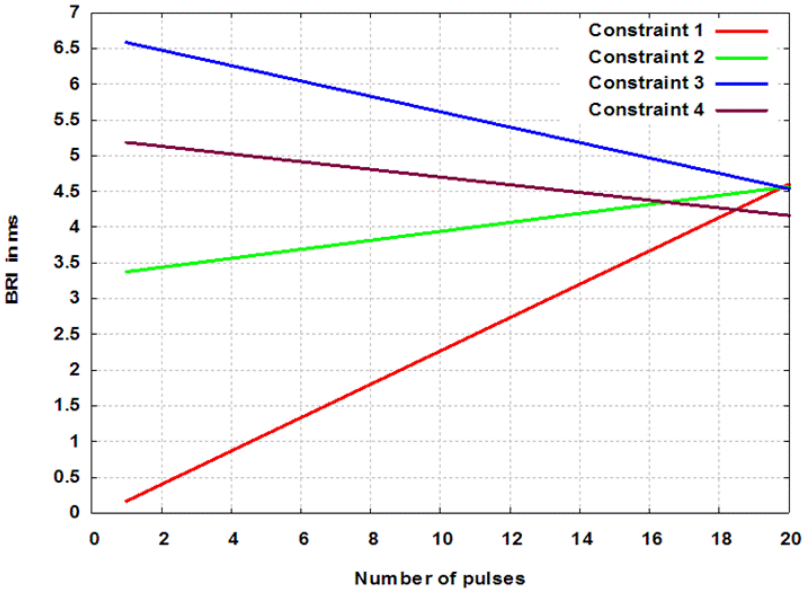

Figure 7. Design-curves of BRI as function of number of pulses in a burst.

5. SPATIAL RESOLUTION

The range –resolution is similar to the real-aperture case and is determined by the bandwidth B_{chirp} of the LFM pulse (or the chirp; refer Equation 27).

$$\partial_{el} = \frac{c}{2B_{chirp} \sin\theta_{inc}} \tag{27}$$

Oscat had 400KHz chirp bandwidth which could yield range-resolution of the order of 0.5km. However, the pulse-compressed spectrum was frequency-binned to generate range-slices of selectable resolution. The nominal range-slice bandwidth was 9.54 KHz which corresponded to 6km elevation resolution [1]. The frequency integration can be dispensed with in the high-resolution Scatterometer to avail of the original 0.5 km range resolution.

The azimuth resolution is improved over the beamwidth limit by the time-bandwidth product (TBP). TBP is the product of the dwell time (τ_{dwell}) over a footprint and its Doppler bandwidth (Δf_{dop}). The beam dwells upon the footprint over the duration of the pulse burst. We have seen in the previous section that one of the crucial factors limiting the BRI and hence, the burst width is the along-scan continuity of the footprint area that is swept by all the pulses in a burst. Therefore, from Equation 25, one can derive the limiting constraint for the burst width (see Equation 28). It appears that the dwell-time or the burst-width is one-third the time the beam would have dwelt due to scanning motion alone. This, in turn causes a factor of 3 degradation in the achievable azimuth resolution. Using Equations 19 and 28, we arrive at the azimuth resolution (see Equation 29) that can be achieved by virtue of Doppler filtering.

$$\tau_{dwell} = T_{burst} \le \frac{1}{3}\frac{R\beta_{az}}{w_{scan}R_g} \tag{28}$$

$$\partial_{az} = \frac{R\beta_{az}}{TBP} = \frac{R\beta_{az}}{\tau_{dwell}\Delta f_{dop}} = \frac{R\beta_{az}}{\left(\frac{1}{3}\frac{R\beta_{az}}{w_{scan}R_g}\right)\left(\frac{2v_{sc}}{\lambda}\beta_{az}\right)} = \frac{3\lambda w_{scan}R_g}{2v_{sc}\beta_{az}} \tag{29}$$

It turns out that if the Oscat beamwidth is improved to 1^0 (~1.5m paraboloid dish), the scan-rate reduced to 16 rpm, the azimuth resolution achievable at Ku-band is of the order of 0.5km at swath-edge. Using the model of resolution degradation across swath discussed in Section 2, one can have the confidence of having better than 5km resolution across 90% of the swath. However, the Range-Doppler ambiguities will be a cause of concern and will require unconventional signal generation and processing schemes.

6. CONCLUSION

A conceptual treatise of the system design approach of high-resolution scanning Scatterometers has been attempted to a fair detail in this paper. ISRO is planning to develop a high-resolution Scatterometer system for one of the missions in its ocean-observing satellite series. The authors wish that the concepts presented in this paper see the light of the day and the global user community gets its first high-resolution scanning Scatterometer.

REFERENCES

[1] Misra T., Chakraborty P., *et al.,* "Oceansat-II Scatterometer: Sensor Performance Evaluation, σ^0 Analyses, and Estimation of Biases," *IEEE Transactions On Geoscience and Remote Sensing*, Volume 52 Issue 6 (2014)

[2] Long D.G., Hardin P.J., Whiting P.T., "Resolution Enhancement of Spaceborne Scatterometer data," *IEEE Transactions On Geoscience and Remote Sensing*, Volume 32 (1994)

[3] Long D.G., *et al.*, "The Design of an Onboard digital Doppler Processor for a Spaceborne Scatterometer *IEEE Transactions On Geoscience and Remote Sensing*, Volume 26 No.6 (1988)